Superstructures and magnetic orders in heavily Cu-substituted $(Fe_{1-x}Cu_x)_{1+y}Te$

Saizheng Cao,[1] Xin Ma,[1] Dongsheng Yuan,[2] Zhen Tao,[3] Xiang Chen,[4,2] Yu He,[5,4,2] Patrick N. Valdivia,[4,2] Shan Wu,[4,2] Hang Su,[1] Wei Tian,[6] Adam A. Aczel,[6] Yaohua Liu,[6,7] Xiaoping Wang,[6] Zhijun Xu,[8,9] Huiqiu Yuan,[1] Edith Bourret-Courchesne,[2] Chao Cao,[1] Xingye Lu,[3] Robert Birgeneau,[4,2] and Yu Song[1,4,2,*]

[1] *Center for Correlated Matter and School of Physics, Zhejiang University, Hangzhou 310058, China*
[2] *Materials Science Division, Lawrence Berkeley National Lab, Berkeley, California 94720, USA*
[3] *Center for Advanced Quantum Studies, Applied Optics Beijing Area Major Laboratory, and Department of Physics, Beijing Normal University, Beijing, China*
[4] *Physics Department, University of California, Berkeley, California 94720, USA*
[5] *Department of Applied Physics, Yale University, New Haven, Connecticut 06511, USA*
[6] *Neutron Scattering Division, Oak Ridge National Laboratory, Oak Ridge, Tennessee 37831, USA*
[7] *Second Target Station, Oak Ridge National Laboratory, Oak Ridge, Tennessee 37831, USA*
[8] *NIST Center for Neutron Research, National Institute of Standards and Technology, Gaithersburg, Maryland 20899, USA*
[9] *Department of Materials Science and Engineering, University of Maryland, College Park, Maryland 20742, USA*

Most iron-based superconductors exhibit stripe-type magnetism, characterized by the ordering vector $\mathbf{Q} = (\frac{1}{2}, \frac{1}{2})$. In contrast, $Fe_{1+y}Te$, the parent compound of the $Fe_{1+y}Te_{1-x}Se_x$ superconductors, exhibits double-stripe magnetic order associated with the ordering vector $\mathbf{Q} = (\frac{1}{2}, 0)$. Here, we use elastic neutron scattering to investigate heavily Cu-substituted $(Fe_{1-x}Cu_x)_{1+y}Te$ compounds and reveal that for $x \gtrsim 0.4$, short-range magnetic order emerges around the stripe-type vector, at $\mathbf{Q} = (\frac{1}{2} \pm \delta, \frac{1}{2} \pm \delta, \frac{1}{2})$ with $\delta \approx 0.05$. We identify the short-range magnetic order to be associated with a phase that exhibits superstructure modulations at $\mathbf{Q} = (\frac{1}{3}, \frac{1}{3}, \frac{1}{2})$, with the correlation length for the magnetic order shorter than that for the superstructure. For $x \gtrsim 0.55$, we observe an additional inter-grown phase with higher Cu-content, characterized by a superstructure modulation vector $\mathbf{Q} = (\frac{1}{3}, \frac{1}{3}, 0)$ and magnetic peaks at $\mathbf{Q} = (\frac{2}{3}, \frac{1}{3}, \frac{1}{2})/(\frac{1}{3}, \frac{2}{3}, \frac{1}{2})$. The positions of the superstructure peaks suggest that relative to the tetragonal unit cell of $Fe_{1+y}Te$, heavy Cu-substitution leads to an expansion of the unit cell by $\sqrt{2} \times 3\sqrt{2}$ times in the *ab*-plane. First-principles calculations suggest the formation of spin chains and spin ladders from Fe-Cu ordering. Our findings show that stripe-type magnetism is common in magnetically diluted iron pnictides and chalcogenides, despite the varying associated atomic orderings.

I. INTRODUCTION

Magnetic fluctuations may facilitate unconventional superconductivity [1], thus the character and origin of magnetism are pivotal issues in understanding unconventional superconductors. For most iron-based superconductors (FeSCs), superconductivity appears in the vicinity of stripe-type antiferromagnetic (AFM) order, characterized by the ordering vector $\mathbf{Q} = (\frac{1}{2}, \frac{1}{2})$ in the two-Fe tetragonal unit cell [Figs. 1(a) and (b)] [2, 3]. In contrast, for the $Fe_{1+y}Te_{1-x}Se_x$ superconductors [4, 5], their parent compound $Fe_{1+y}Te$ exhibits bicollinear magnetic order with the ordering vector $\mathbf{Q} = (\frac{1}{2}, 0)$ [Fig. 1(b)] [6, 7]. The stripe-type magnetism in the FeSCs may arise from the nesting of Fermi surfaces [8, 9] or local-moments that exhibit frustrated magnetic interactions [10], whereas an interplay between local-moments and itinerant carriers is suggested to be important for understanding the magnetism in $Fe_{1+y}Te$ [11].

The magnetism of FeSC parent compounds such as $BaFe_2As_2$ and NaFeAs can be effectively tuned via doping on the Fe site. For example, Co- and Ni-substitution leads to electron-doping and results in the suppression of AFM order and the emergence of superconductivity [12, 13]. The effect of Cu-substitution is more complex. At low substitution levels, in addition to electron-doping and suppressing AFM order, the Cu atoms also lead to strong impurity potentials [14, 15] and weakened superconductivity [16, 17]. With increasing Cu substitution level, the electron-doping contributed per Cu decreases [15, 18], and the Cu dopants eventually become nonmagnetic and no longer contribute to the electronic density of states at the Fermi level [19].

In heavily Cu-substituted $NaFe_{1-x}Cu_xAs$, a correlated insulator appears for $x \gtrsim 0.2$ [20–23], accompanied by Fe-Cu ordering into chains and magnetic order at $\mathbf{Q} = (\frac{1}{2}, \frac{1}{2})$ [Fig. 1(c)] [22, 24]. In $Ba(Fe_{1-x}Cu_x)_2As_2$, ω/T scaling is found near a putative AFM quantum critical point at $x = 0.043$ [25], and short-range AFM order at the stripe-type vector reemerges for $x \gtrsim 0.15$, accompanied by insulating-like electrical transport, without detectable Fe-Cu ordering [26]. In the case of $(Fe_{1-x}Cu_x)_{1+y}Te$ (FCT), AFM order at the double-stripe vector $(\frac{1}{2}, 0)$ becomes suppressed for $x \approx 0.1$ [27] while a spin glass state with insulating-like electrical transport appears for larger Cu content (up to $x \approx 0.5$) [28, 29]. Whether the spin glass state in FCT is associated with short-range magnetic order (mSRO), and whether heavy Cu-substitution in FCT leads to Fe-Cu ordering as in $NaFe_{1-x}Cu_xAs$, are yet unclear.

In this work, we examine these issues using elastic neutron diffraction and first-principles calculations.

We find that FCT with $x \gtrsim 0.4$ exhibits mSRO at $\mathbf{Q} = (\frac{1}{2} \pm \delta, \frac{1}{2} \pm \delta, L)$, with $\delta \approx 0.05$ and half-integer-L. The mSRO is associated with a superstructure modulation at half-integer-L $(\frac{1}{3}, \frac{1}{3})$ positions [Fig. 1(d)]. For $x \gtrsim 0.55$, we discover an inter-grown phase with superstructure peaks at integer-L $(\frac{1}{3}, \frac{1}{3})$ positions, and magnetic peaks at half-integer-L $(\frac{1}{3}, \frac{2}{3}, L)/(\frac{2}{3}, \frac{1}{3}, L)$ positions [Fig. 1(e)]. Possible structural models consistent with the observed superstructure peaks are studied using first-principles calculations, suggesting candidate phases with Fe-Cu ordering into chains or ladders. These results suggest three phases in the phase diagram of FCT, one without Fe-Cu ordering (FCT I), one with a superstructure modulated by half-integer-L $(\frac{1}{3}, \frac{1}{3})$ (FCT II), and one with a superstructure modulated by integer-L $(\frac{1}{3}, \frac{1}{3})$ (FCT III) [Fig. 1(f)]. Our findings suggest that stripe-type magnetism is common in magnetically-diluted iron pnictides and chalcogenides, despite the varied atomic orderings (or lack thereof) in different systems. Moreover, the tendency towards atomic ordering in these magnetically diluted materials provides a pathway for the study of correlated electrons in quasi-one-dimensional and cluster systems.

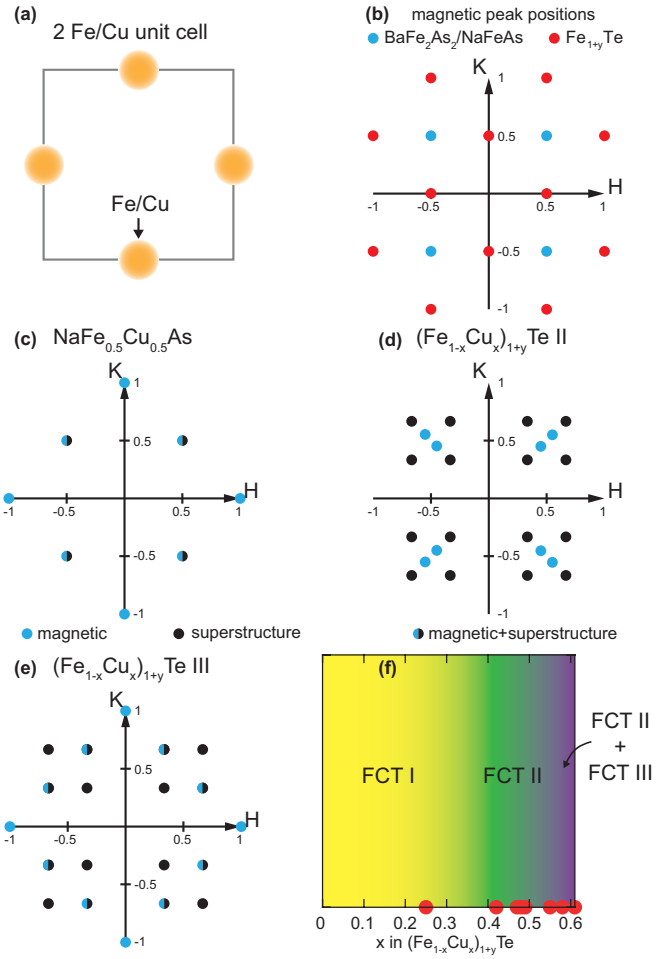

FIG. 1. (a) 2-Fe unit cell of the FeSCs. With Cu-substitution, the Fe site may be occupied by either Fe or Cu. (b) Schematic comparison of magnetic peak positions in $BaFe_2As_2$/NaFeAs and $Fe_{1+y}Te$. Schematic diagrams for the positions of magnetic and superstructure peaks in (c) $NaFe_{0.5}Cu_{0.5}As$, (d) $(Fe_{1-x}Cu_x)_{1+y}Te$ II, and (e) $(Fe_{1-x}Cu_x)_{1+y}Te$ III. (f) The schematic phase diagram for $(Fe_{1-x}Cu_x)_{1+y}Te$ (FCT). FCT I does not exhibit superstructure peaks, FCT II exhibits $(\frac{1}{3}, \frac{1}{3}, \frac{1}{2})$ superstructure peaks, and FCT III exhibits $(\frac{1}{3}, \frac{1}{3}, 0)$ superstructure peaks. For $x \gtrsim 0.55$, FCT II and III are inter-grown. The red circles represent samples studied in this work. The y-axis does not correspond to a physical quantity.

II. METHODS

A. Experimental details

Single crystals of $(Fe_{1-x}Cu_x)_{1+y}Te$ were synthesized using the modified Bridgeman method [29, 30]. A series of samples were synthesized at Beijing Normal University with the nominal compositions $y_{\text{nom}} = 0.1$ and $x_{\text{nom}} = 0.2, 0.3, 0.4, 0.5$, and 0.6 (Growth A). Samples with the nominal composition $x_{\text{nom}} = 0.5$ and $y_{\text{nom}} = 0.1$ were synthesized at the Lawrence Berkeley National Laboratory (Growth B). Two samples from Refs. [29, 30] (Growth C) were also studied in this work. The electrical resistivity $\rho(T)$ of samples from Growth A were measured using the standard four-probe method.

The samples' compositions were determined using energy-dispersive spectroscopy (EDS), by assuming a full occupancy of the Te site. The resulting values of x and y, as determined from EDS, are summarized in Table. I, together with a summary of superstructure and magnetic peaks. Multiple points on each sample were probed, and the standard deviation between different points are used to estimate the uncertainties of x and y. Compared to samples from Growth B and C, those from Growth A have a higher occupation of the interstitial site (larger values of y). In this work, we reference the values of x and y determined from EDS measurements.

Elastic neutron scattering measurements on samples from Growth A were carried out using the Fixed-Incident Energy Triple-Axis Spectrometer (HB-1A) at the High-Flux Isotope Reactor (HFIR), Oak Ridge National Laboratory (ORNL). Consistent experimental setups are used in these measurements, and the measured intensities are reported in arbitrary units after normalization by the sample mass. Samples from Growth B were studied on the Elastic Diffuse Scattering Spectrometer (CORELLI) and the Single-Crystal Diffractometer (TOPAZ) at the Spallation Neutron Source (SNS), ORNL. The CORELLI and TOPAZ data were transformed into the 3D reciprocal space via the standard reduction algorithm available at the beamlines. Samples from Growth C were studied using the Double-Focusing Triple-Axis Spectrometer (BT-7) at the NIST Center for Neutron Research (NCNR) and HB-1A at the HFIR. The measured intensities of samples from Growths B and C are reported in arbitrary units.

Growth	$x_{\rm nom}$	$y_{\rm nom}$	x	y	$(\frac{1}{3},\frac{1}{3},\frac{1}{2})$-type superstructure	$(\frac{1}{3},\frac{1}{3},0)$-type superstructure	$(\frac{1}{2}\pm\delta,\frac{1}{2}\pm\delta,\frac{1}{2})$-type mSRO	$(\frac{1}{3},\frac{2}{3},\frac{1}{2})$-type magnetic order
A	0.2	0.1	0.25(2)	0.20(3)	×	×	×	—
A	0.3	0.1	0.42(1)	0.24(4)	✓	×	✓	—
A	0.4	0.1	0.48(3)	0.30(5)	✓	×	✓	—
A	0.5	0.1	0.58(2)	0.37(3)	✓	✓	✓	—
A	0.6	0.1	0.61(1)	0.32(3)	✓	✓	✓	—
B	0.5	0.1	0.55(1)	0.20(3)	✓	✓	✓	✓
C	0.46	0.08	0.49(5)	0.22(3)	✓	—	✓	—
C	0.42	0.18	0.47(3)	0.22(3)	✓	—	✓	—

TABLE I. The nominal and measured sample compositions for FCT samples studied in this work. The compositions for samples from Growth C are from Ref. [29]. The superstructure and magnetic peaks are also summarized for comparison, with the symbols ✓ and × respectively corresponding to their presence and absence. The — symbol corresponds to peaks that were not examined in this study.

B. First-principles calculations

To study the possible superstructures of FCT, we performed first-principles density functional theory (DFT) simulations as implemented in the `VASP` package [31, 32]. The ion-electron interactions were approximated with the projected augmented wave (PAW) method [32, 33], and the Perdew, Burke and Enzerhoff (PBE) flavor of generalized gradient approximation to the exchange-correlation functional were chosen [34]. The energy cutoff of plane-wave basis was set to 590 eV, and Γ centered k-meshes with spacing less than 0.02 Å^{-1} were used to perform the integration of the Brillouin zone. All lattice constants and internal atomic coordinates were fully relaxed until forces on each atom is smaller than 0.001 eV/Å. Since we are interested in the formation of superstructures during sample crystallization, which takes place at temperatures much higher than $T_{\rm N}$, magnetism and spin-orbit coupling were not considered in our calculations.

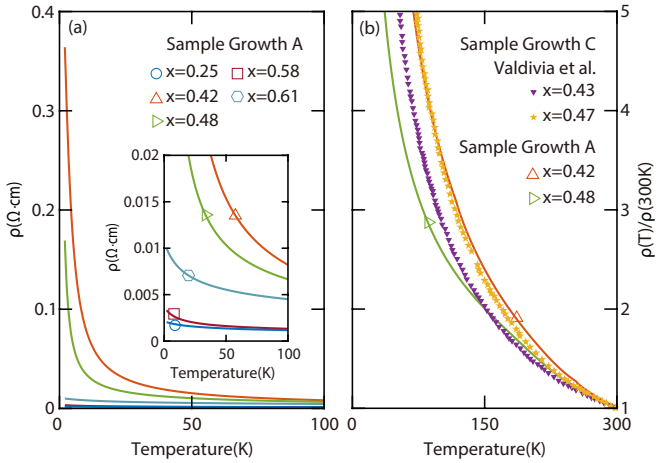

FIG. 2. (a) In-plane electrical resistivity $\rho(T)$ for FCT samples. The inset zooms in around low temperatures. (b) Comparison of $\rho(T)/\rho(300\ {\rm K})$ for FCT samples from Growths A and C [29].

III. RESULTS

A. Electrical transport of FCT

Electrical resistivity for FCT samples with $x \gtrsim 0.25$ (Growth A) are shown in Fig. 2(a), with semiconducting behaviors observed in all cases. FCT becomes more insulating as x increases from 0.25 to 0.42 and 0.48, but then becomes less insulating as x is further increased to 0.58 and 0.61. The evolution of electrical transport in Fig. 2(a) is broadly consistent with results in Ref. [29], which finds that FCT becomes more insulating with increasing Cu-content up to $x \approx 0.47$. This broad consistency is also seen in the similar behaviors of $\rho(T)/\rho(300\ {\rm K})$ for FCT samples (with x between 0.42 and 0.48) from Growths A and C [Fig. 2(b)].

B. mSRO in FCT

Figs. 3(a) and (b) show elastic scans along $(H, H, \frac{3}{2})$ for FCT samples with $x = 0.48$ and 0.61 (Growth A), at both 5 K and $T > 200$ K. As can be seen, a pair of broad peaks centered around $(\frac{1}{2}, \frac{1}{2}, \frac{3}{2})$ are present at 5 K, which vanish when $T > 200$ K. The 5 K data, with the corresponding $T > 200$ K data subtracted as background, are shown in Fig. 3(c) for $x = 0.42$, 0.48, 0.58 and 0.61, and reveal the presence of similar mSRO in all these samples. A $x = 0.25$ sample was also studied, but no detectable magnetic peaks were found. Given Cu becomes nonmagnetic in heavily Cu-substituted $Sr(Fe_{1-x}Cu_x)_2As_2$ [19] and $NaFe_{1-x}Cu_xAs$ [22], we assume that Cu is nonmagnetic in FCT samples with $x \gtrsim 0.4$, and collective magnetism such as the mSRO arise from Fe.

The data in Fig. 3(c) are well described by two

Lorentzian peaks centered around $(\frac{1}{2}, \frac{1}{2}, \frac{3}{2})$:

$$I(\mathbf{Q}) = \frac{A_1}{[H-(\frac{1}{2}-\delta_1)]^2+\kappa^2} + \frac{A_2}{[H-(\frac{1}{2}+\delta_2)]^2+\kappa^2}, \quad (1)$$

where A_i are the intensity scale factors for the two peaks, δ_i are the shifts from $(\frac{1}{2}, \frac{1}{2})$ along the in-plane longitudinal direction, and κ is the half-width-at-half-maximum (HWHM) of the Lorentzian peaks. κ is related to the correlation length through $\xi_{110} = a/(\sqrt{2}\pi\kappa)$, where the factor of $\sqrt{2}$ rather than 2 is due to the scan being along the (110) direction. The fit values δ_1 and δ_2 are similar, with an average value $\delta = (\delta_1+\delta_2)/2 \approx 0.05$. Scans along L centered on the right peak in Fig. 3(c) are presented in Fig. 3(d), revealing a single peak centered at $L = \frac{3}{2}$ for each sample. These L-scans are well-described by a single Lorentzian peak, and the correlation length can be extracted via $\xi_c = c/(2\pi\kappa)$. We note instrumental resolution was not considered in our analysis, so the fit κ are upper limits, and the corresponding correlation lengths are lower limits.

The temperature dependence of the magnetic intensity at $(\frac{1}{2}+\delta, \frac{1}{2}+\delta, \frac{3}{2})$ are shown in Fig. 3(e), revealing a gradual onset of magnetic intensity below $T \approx 170$ K. Fig. 3(f) shows that the scaled temperature dependence overlap for different samples. This contrasts with behaviors found in $NaFe_{1-x}Cu_xAs$, where the temperature dependence of the magnetic intensity varies significantly with Cu substitution level [22].

The mSRO is also studied for a $x = 0.47$ FCT sample from Growth C, with the 4.5 K data in multiple Brillouin zones shown in Figs. 4(a)-(d), after subtracting the 200 K data. In all cases, a pair of diffuse peaks are observed at positions equivalent to $(\frac{1}{2} \pm \delta, \frac{1}{2} \pm \delta, \frac{1}{2})$. In Figs. 4(a) and (c), the intensities of the two peaks are highly asymmetric, and is not captured by the magnetic form factor alone. It is interesting that the maximum intensity occurs at $L = \frac{3}{2}$ rather than $L = \frac{1}{2}$, further confirmed in the scan along $(0.55, 0.55, L)$ [Fig. 4(f)]. We find that the momentum dependence of magnetic intensity in Fig. 4(f) is reasonably described by a lattice sum of Lorentzian functions polarized along the in-plane longitudinal (110) direction (red dashed line):

$$I(\mathbf{Q}) = f(Q)^2(1-Q_{110}^2/Q^2) \sum_{i=-\infty}^{\infty} \frac{A}{(L-(i+\frac{1}{2}))^2+\kappa^2}, \quad (2)$$

where A is an intensity scale factor, $f(Q)$ is the Fe^{2+} magnetic form factor, Q_{110} is the component of the momentum transfer along the (110) direction, $(1-Q_{110}^2/Q^2)$ is the polarization factor, and κ is the HWHM of the Lorentzian peaks. The scans along (110) in Figs. 4(a)-(d) are also reasonably described by a similar model (red dashed lines):

$$I(\mathbf{Q}) = f(Q)^2(1-Q_{110}^2/Q^2)\times \sum_{i=-\infty}^{\infty} \frac{A}{(H-(i+\frac{1}{2}-\delta))^2+\kappa^2} + \frac{A}{(H-(i+\frac{1}{2}+\delta))^2+\kappa^2}. \quad (3)$$

The observation that the elastic magnetic signal in FCT can be reasonably modeled by Eqs. 2 and 3 suggest that the spins are dominantly polarized along the in-plane longitudinal direction, similar to the stripe-type magnetic order in the FeSCs [2].

Figs. 4(a)-(d) unequivocally demonstrate that the mSRO in FCT is split along the in-plane longitudi-

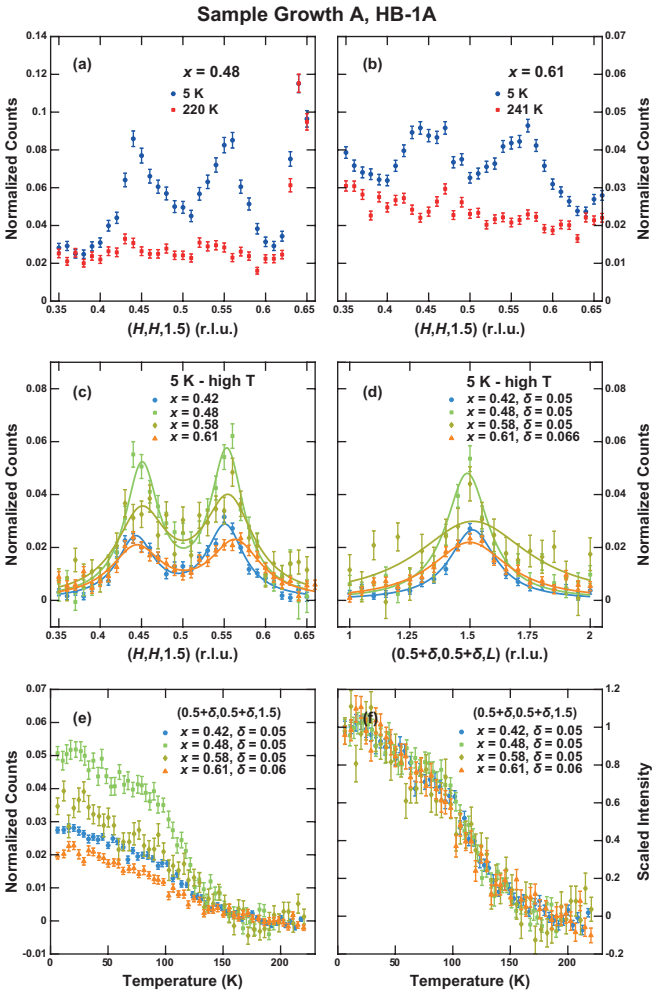

FIG. 3. Scans along $(H, H, \frac{3}{2})$ for FCT with (a) $x = 0.48$ and (b) $x = 0.61$ at 5 K and $T > 200$ K. (c) $(H, H, \frac{3}{2})$ and (d) $(\frac{1}{2}+\delta, \frac{1}{2}+\delta, L)$ scans for FCT, subtracted by the corresponding high temperature data ($T = 220$ K for $x = 0.42$ and 0.48, $T = 241$ K for $x = 0.58$ and 0.61). (e) Temperature dependence of the elastic intensity at $(\frac{1}{2}+\delta, \frac{1}{2}+\delta, \frac{3}{2})$ for FCT, the average of data at $T \geq 170$ K have been subtracted as background. (f) The data in panel (e) are scaled together by further dividing the average of data with $T \leq 30$ K.

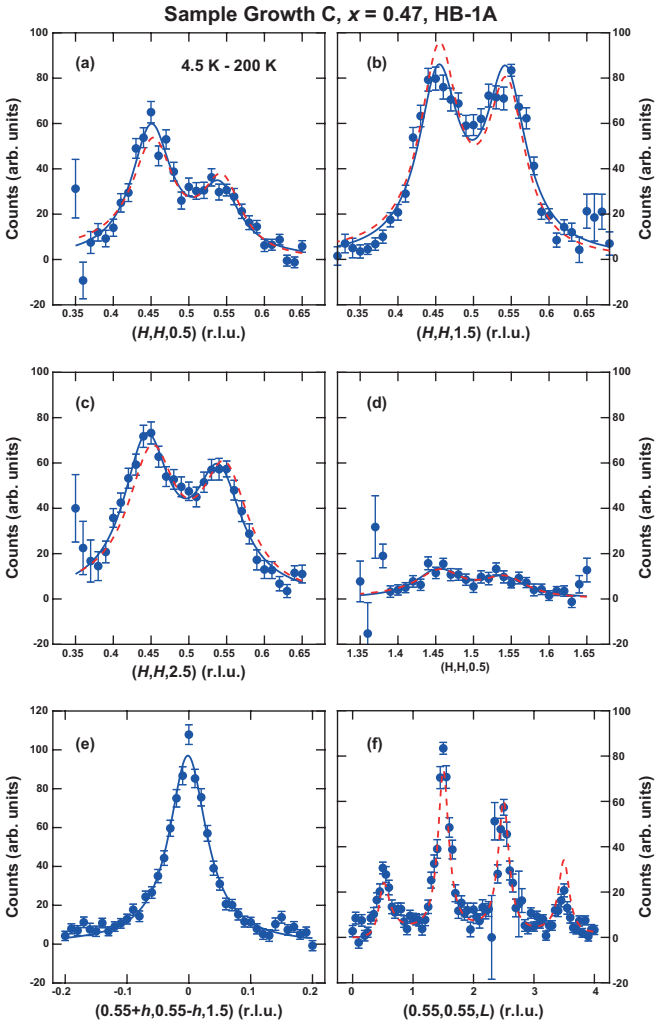

FIG. 4. Scans for a $x = 0.47$ FCT sample along [110] centered at (a) $(\frac{1}{2}, \frac{1}{2}, \frac{1}{2})$, (b) $(\frac{1}{2}, \frac{1}{2}, \frac{3}{2})$, (c) $(\frac{1}{2}, \frac{1}{2}, \frac{5}{2})$, and (d) $(\frac{3}{2}, \frac{3}{2}, \frac{1}{2})$. (e) Scan along $[1\bar{1}0]$ centered at $(0.55, 0.55, \frac{3}{2})$ for the $x = 0.47$ FCT sample. (f) $(0.55, 0.55, L)$ scan for the $x = 0.47$ FCT sample over a large L-range. All scans are measured at 4.5 K, and the corresponding 200 K scan have been subtracted as background. The solid lines are fits to Eq. 1 or a single Lorentzian peak, the dashed line in (f) is a fit to Eq. 2, and the dashed lines in (a)-(d) are fits to Eq. 3.

nal direction, forming two peaks at $(\frac{1}{2} \pm \delta, \frac{1}{2} \pm \delta)$ with $\delta \approx 0.05$. To examine whether a similar splitting of magnetic peaks occurs along the in-plane transverse direction, we mounted the $x = 0.47$ sample in the $[113] \times [1\bar{1}0]$ scattering plane, which in combination with a small tilt of the sample table allows the $(0.55 + h, 0.55 - h, 1.5)$ scan to be carried out. As can be seen in Fig. 4(e), in contrast to the in-plane longitudinal direction, a single peak is observed along the in-plane transverse direction.

Based on data in Figs. 3 and 4, we find that the mSRO peaks in FCT are split by $\delta \approx 0.05$ along the in-plane longitudinal direction, but are centered at half-integer positions along the in-plane transverse direction and along L,

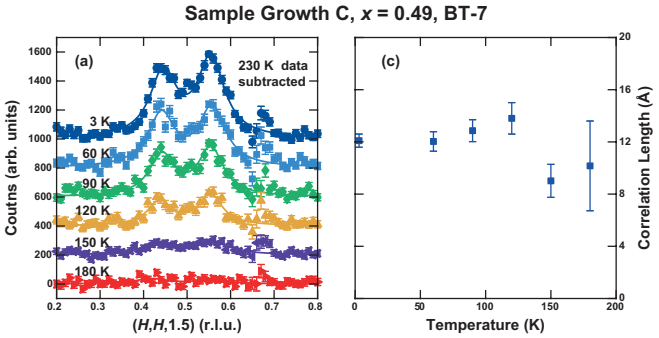

FIG. 5. (a) Scans along [110] centered at $(\frac{1}{2}, \frac{1}{2}, \frac{3}{2})$ for a $x = 0.49$ sample at various temperatures, with the 230 K data subtracted as background. The data have been shifted vertically for clarity. (b) The temperature evolution of the correlation length, obtained by fitting the data in panel (a) to Eq. 1.

as schematically depicted in Fig. 1(d). We note mSROs with peaks transversely split around $(\frac{1}{2}, \frac{1}{2})$ are observed in Co- and Ni-doped $BaFe_2As_2$ [35, 36].

Scans along $(H, H, \frac{3}{2})$ at various temperatures are carried out for a $x = 0.49$ sample (Growth C), with results shown in Fig. 5(a). As can be seen, the peak shape hardly changes with temperature. By fitting the data in Fig. 5(a) to Eq. 1, we find an essentially temperature-independent correlation length of ≈ 10 Å [Fig. 5(b)].

C. Superstructure in FCT

Motivated by the observation of superstructure peaks at half-integer-L $(\frac{1}{2}, \frac{1}{2})$ positions in $NaFe_{1-x}Cu_xAs$ [Fig. 1(c)], we searched for superstructure peaks in FCT along high symmetry directions, with findings summarized in Figs. 6 and 7. In Fig. 6, scans along [110] centered around $(\frac{1}{3}, \frac{1}{3}, L)$ and $(\frac{2}{3}, \frac{2}{3}, L)$, with $L = 0$ and $\frac{1}{2}$, are shown for FCT samples with $x = 0.42$, 0.48, 0.58, and 0.61 (Growth A). For $x = 0.42$ and 0.48, clear superstructure peaks are observed at $(\frac{1}{3}, \frac{1}{3}, \frac{1}{2})$ and $(\frac{2}{3}, \frac{2}{3}, \frac{1}{2})$ positions, whereas little or no intensity is seen at $L = 0$ positions [Figs. 6(a)-(d)]. While a small peak is seen at $(\frac{1}{3}, \frac{1}{3}, 0)$ in the $x = 0.42$ sample, a scan along L reveals that it is in fact associated with a scattering rod [Fig. 7(a)]. Therefore, we conclude that in the $x = 0.42$ and 0.48 samples, the superstructure peaks are observed at half-integer-L $(\frac{1}{3}, \frac{1}{3})$ and $(\frac{2}{3}, \frac{2}{3})$ positions.

For the $x = 0.58$ and 0.61 samples, in addition to the half-integer-L superstructure peaks, integer-L superstructure peaks are also observed, although with in-plane momenta slightly smaller than $(\frac{1}{3}, \frac{1}{3})$ and $(\frac{2}{3}, \frac{2}{3})$ [Figs. 6(e)-(h)]. We rule out this being an incommensurate structural modulation, since in such a case the peaks should be at $(\frac{1}{3} - \epsilon, \frac{1}{3} - \epsilon)$ and $(\frac{2}{3} + \epsilon, \frac{2}{3} + \epsilon)$, inconsistent with the experimental observation. As will be discussed below, these are in fact integer-L $(\frac{1}{3}, \frac{1}{3})$ and $(\frac{2}{3}, \frac{2}{3})$ superstructure peaks associated with an inter-grown phase.

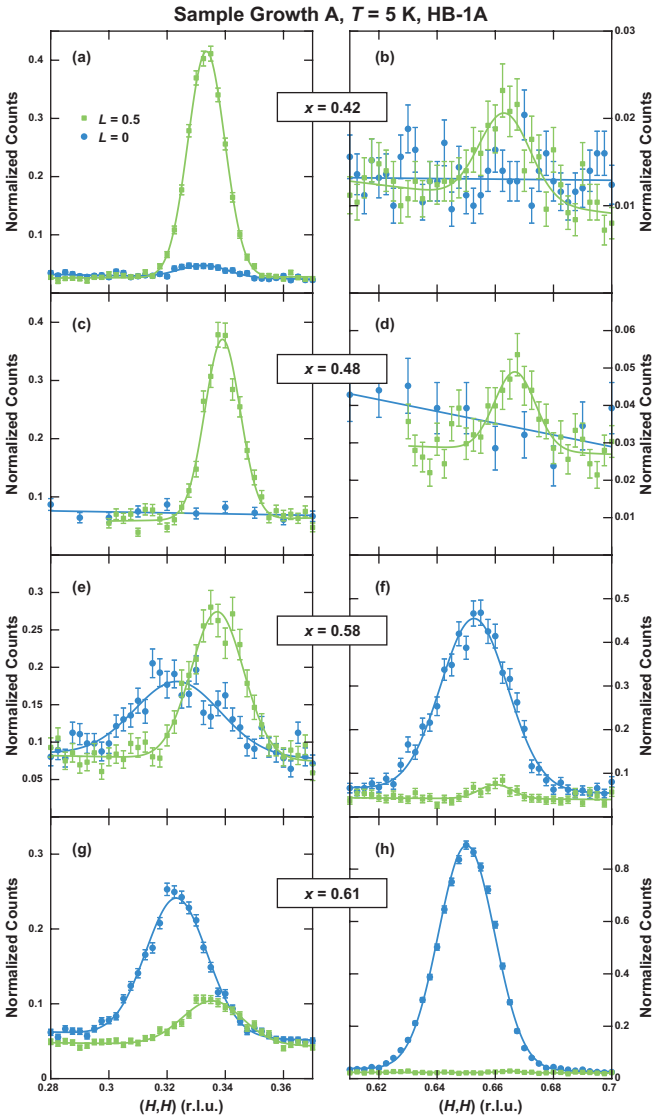

FIG. 6. Scans at 5 K along [110] around $\mathbf{Q} = (\frac{1}{3}, \frac{1}{3}, L)$, for FCT samples with (a) $x = 0.42$, (c) $x = 0.48$, (e) $x = 0.58$, and (g) $x = 0.61$. Similar scans around $\mathbf{Q} = (\frac{2}{3}, \frac{2}{3}, L)$ are shown in panels (b), (d), (f) and (g). The solids lines are fits to Gaussian peaks on linear backgrounds.

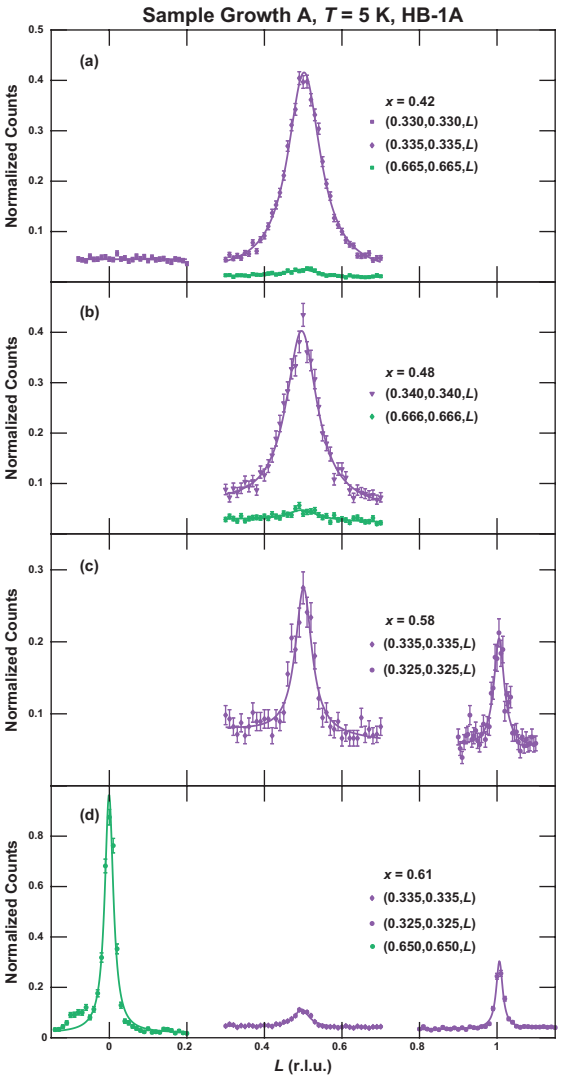

FIG. 7. L-scans of superstructure peaks at 5 K in FCT samples with (a) $x = 0.42$, (b) $x = 0.48$, (c) $x = 0.58$, and (d) $x = 0.61$. The solids lines are fits to Lorentzian peaks on linear backgrounds.

With the increase in x, these integer-L $(\frac{1}{3}, \frac{1}{3})$ superstructure peak gains intensity, suggesting an increase in the volume fraction of the inter-grown phase.

Our observation of superstructure peaks is corroborated by L-scans shown in Fig. 7. In the $x = 0.42$ sample, clear peaks are observed at $(\frac{1}{3}, \frac{1}{3}, \frac{1}{2})$ and $(\frac{2}{3}, \frac{2}{3}, \frac{1}{2})$, although the latter is much weaker [Fig. 7(a)]. These peaks are also observed in the $x = 0.48$ sample [Fig. 7(b)]. On the other hand, the L-scan across $(\frac{1}{3}, \frac{1}{3}, 0)$ in the $x = 0.42$ FCT sample is completely flat [Fig. 7(a)], despite the presence of a peak in the scan along [110] [Fig. 6(a)]. This suggests the integer-L peak in the scan along [110] in Fig. 6(a) results from a scattering rod, evidencing the presence of stacking faults associated with the $(\frac{1}{3}, \frac{1}{3}, \frac{1}{2})$ superstructure. In the $x = 0.58$ and 0.61 samples, superstructure peaks are observed in L-scans at both integer-L and half-integer-L positions [Figs. 7(c) and (d)], consistent with observations in Fig. 6.

The superstructure peaks in Figs. 6 and 7 are scaled to unit height and overplotted in Fig. 8, centered at the fit peak positions. As can be seen, upon increasing x from 0.48 to 0.58, the half-integer-L $(\frac{1}{3}, \frac{1}{3})$ peak broadens along the [110] direction, while a sharpening along L is observed [Figs. 8(a) and (b)]. In comparison, the peak widths along the two directions changes very little when x is increased from 0.42 to 0.48, and from 0.58 to 0.61. For the integer-L $(\frac{1}{3}, \frac{1}{3})$ peak, which is only observed in the $x = 0.58$ and 0.61 samples, the peak is found to sharpen along both [110] and L directions with the increase of x [Figs. 8(c) and (d)].

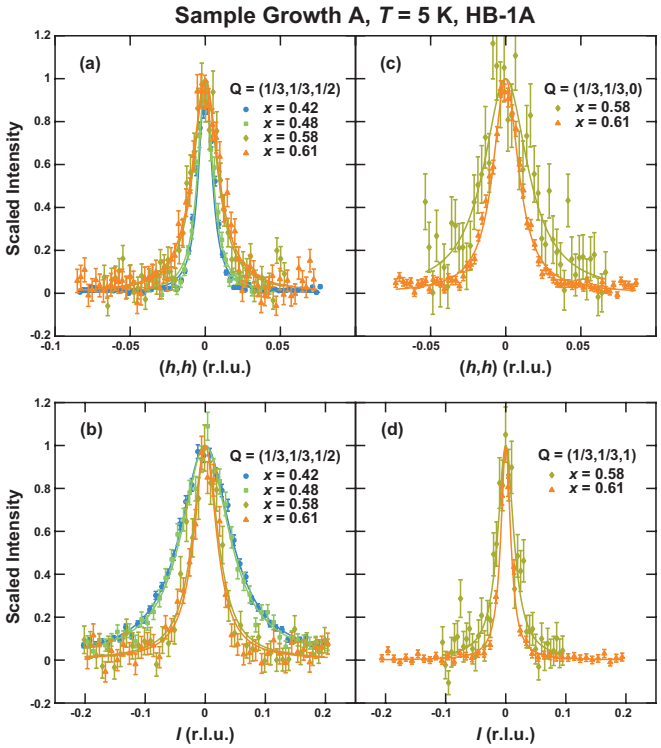

FIG. 8. A comparison of the superstructure peak widths at 5 K in FCT samples, for scans along (a) [110] and (b) L for the half-integer-L superstructure peaks, and scans along (c) [110] and (d) L for the integer-L superstructure peaks. All peaks are fit to a single Lorentzian peak on a linear background, shown as the solid lines. In these plots, the x-axis is subtracted by the fit peak center, the y-axis is subtracted by the fit background, and the maximum intensity is scaled to unity.

The appearance of integer-L peaks near $(\frac{1}{3},\frac{1}{3})$ and $(\frac{2}{3},\frac{2}{3})$ in the $x = 0.58$ and 0.61 samples, and the fact these peaks are positioned at slightly smaller in-plane momenta compared to the half-integer-L superstructure peaks, suggest that they may be associated with an inter-grown phase (FCT III) that emerges with increasing x. To investigate this possibility, a scan along [110] centered at $(2,2,0)$ is presented in Fig. 9(a) for the $x = 0.61$ sample, revealing a smaller side peak centered around $(1.94,1.94,0)$. A rocking scan centered at $(1.945,1.945,0)$ [inset of Fig. 9(a)] excludes this peak being associated with aluminum sample holders or a misaligned grain, and instead evidences an inter-grown phase (FCT III) with similar lattice parameters and the same orientation as the main phase (FCT II). Since the $(2,2,0)$ peak for the inter-grown phase appears at a smaller in-plane momentum compared to the main phase, it has a larger in-plane d-spacing (by $\sim 3\%$). When the integer-L superstructure peaks in Fig. 6 are indexed using the larger in-plane lattice parameter of the inter-grown phase, they are identified as $(\frac{1}{3},\frac{1}{3})$ and $(\frac{2}{3},\frac{2}{3})$ peaks.

To examine whether the inter-grown phase (FCT III)

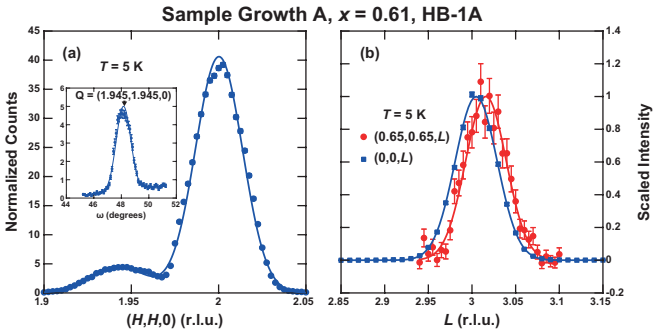

FIG. 9. (a) Longitudinal scan around the $(2,2,0)$ peak for a $x = 0.61$ FCT sample at 5 K. The solid line is a fit to the sum of two Gaussian peaks on a linear background. The inset shows a rocking scan centered at $(1.945,1.945,0)$, and the solid line is a fit to a Gaussian peak on a linear background. (b) Comparison of L-scans at $(0,0,3)$ and $(0.65,0.65,3)$ for the $x = 0.61$ FCT sample. The solid lines are fits to Gaussian peaks on linear backgrounds, the fit backgrounds are subtracted and the maximum intensities are scaled to unity.

also exhibits a different c-axis lattice parameter compared to the main phase (FCT II), a longitudinal scan centered at $(0,0,3)$ is carried out in the $x = 0.61$ sample [blue square symbols in Fig. 9(b)], revealing an absence of detectable side peaks. On the other hand, a L-scan centered on an integer-L superstructure peak associated with FCT III [red circle symbols in Fig. 9(b)] reveals that it is centered at a slightly larger L-value, compared to the $(0,0,3)$ peak. Assuming that the $(0,0,3)$ peak is dominated by the main phase (FCT II), we estimate that the out-of-plane d-spacing for FCT III is $\sim 0.4\%$ smaller than that of FCT II. A larger in-plane d-spacing and a smaller out-of-plane d-spacing suggest that FCT III has a larger Cu-content compared to FCT II, based on the evolution of lattice parameters with Cu-content in $NaFe_{1-x}Cu_xAs$ [22] and $Sr(Fe_{1-x}Cu_x)_2As_2$ [19].

These results suggest the presence of three different phases in FCT, one that does not exhibit any superstructures (FCT I), one with the half-integer-L $(\frac{1}{3},\frac{1}{3})$ superstructure (FCT II), and one with the integer-L $(\frac{1}{3},\frac{1}{3})$ superstructure (FCT III). FCT I persists up to at least $x = 0.25$ without detectable superstructure peaks, FCT II appears for $x \gtrsim 0.4$, and FCT III is inter-grown with FCT II for $x \gtrsim 0.55$. These findings are summarized in Table. I and are shown schematically in Fig. 1(f). Comparing Fig. 1(f) with the evolution of $\rho(T)$ in Fig. 2 suggests while all FCT phases with $x \gtrsim 0.25$ are semiconducting, FCT II is more insulating than FCT I and FCT III.

D. Reciprocal space maps for a $x = 0.55$ FCT sample

To further probe the mSRO and superstructure peaks in FCT, a $x = 0.55$ sample (Growth B) was studied using

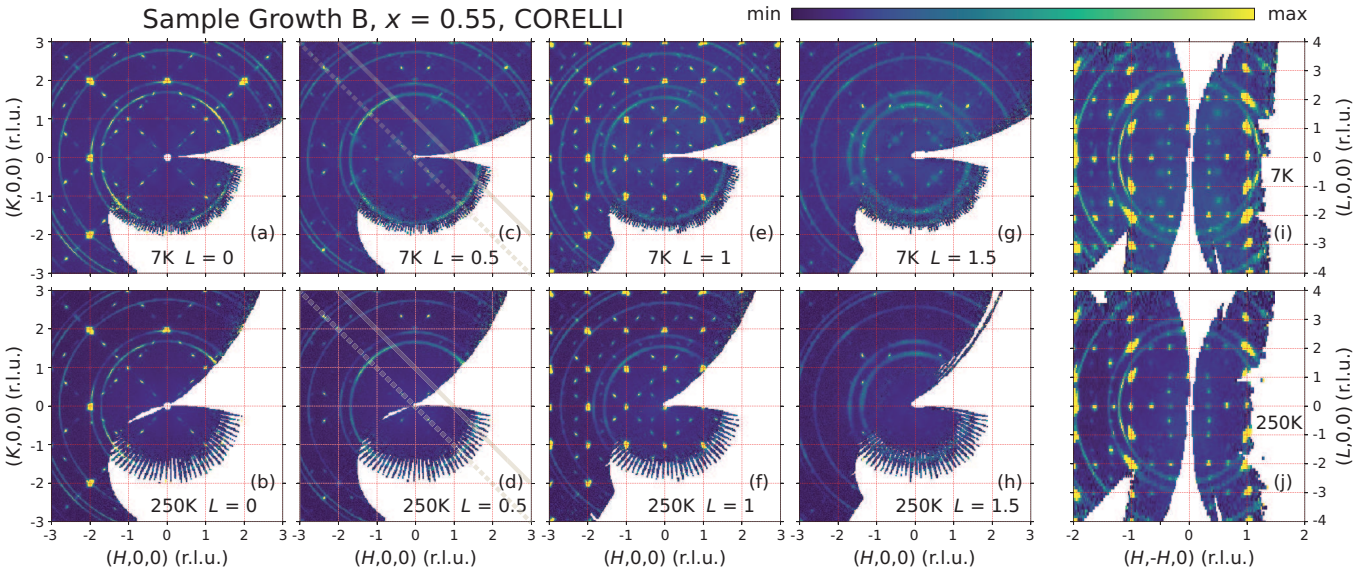

FIG. 10. Diffraction data of a $x = 0.55$ FCT sample measured using CORELLI, with the 7 K (H, K)-maps at $L = 0$, $\frac{1}{2}$, 1, and $\frac{3}{2}$ respectively shown in panels (a), (c), (e), and (g). The corresponding (H, K)-maps at 250 K are respectively shown in panels (b), (d), (f) and (h). (i) and (j) show the $(H, -H, L)$-maps at 7 K and 250K, respectively. Panels (a)-(h) are obtained by binning data $L \pm 0.1$ within the central L-value, and panels (i) and (j) are obtained by binning (H, H) within $\pm(0.025, 0.025)$. Peaks that fall on the dashed gray bands in (c) and (d) do not change significantly with temperature, whereas those on the solid gray bands do.

CORELLI, with results summarized in Fig. 10. Comparing the integer-L (H, K)-maps at 7 K and 250 K [Figs. 10(a), (b), (e), (f)], it can be seen that the integer-L $(\frac{1}{3}, \frac{1}{3})$ peaks (associated with FCT III) are present across multiple Brillouin zones, do not change significantly in intensity upon warming, and do not weaken at large momentum transfers. These observations confirm that they are superstructure (rather than magnetic) peaks.

Furthermore, the integer-L (H, K)-maps clearly reveal that the $(\frac{1}{3}, \frac{1}{3})$ and $(\frac{1}{3}, -\frac{1}{3})$ peaks have distinct shapes, with the $(\frac{1}{3}, \frac{1}{3})$ peaks more elongated along the [110] direction, and the $(\frac{1}{3}, -\frac{1}{3})$ peaks more elongated along the $[1\bar{1}0]$ direction. This difference in peak shape, which is consistently observed across multiple Brillouin zones, suggest that the superstructure modulation does not exhibit fourfold rotational symmetry. Instead, the apparent four-fold rotational symmetry of the diffraction data results from the twinning of superstructures that exhibit two-fold rotational symmetry, similar to the twinning of AFM/orthorhombic domains in the FeSCs [2].

The CORELLI data further reveal the half-integer-L $(\frac{1}{3}, \frac{1}{3})$ and $(\frac{1}{3}, -\frac{1}{3})$ peaks (associated with FCT II) also have anisotropic peak shapes [Figs. 10(c), (d), (g), (h)], exactly like the integer-L superstructure peaks associated with FCT III. The common anisotropy in superstructure peak shapes for FCT II and FCT III indicates that both superstructures form anisotropic domains.

Our results reveal remarkable similarities for FCT II and FCT III, both phase exhibit (i) superstructure modulations with the same in-plane ordering vector $\mathbf{Q} = (\frac{1}{3}, \frac{1}{3})$, (ii) two-fold rotational symmetry, and (iii) domain lengths that are shorter along the ordering vector. For example, the observation that $(\frac{1}{3}, \frac{1}{3})$ peaks are broader along [110] than along $[1\bar{1}0]$ suggests the typical size of the corresponding domain is shorter along [110] compared to along $[1\bar{1}0]$, and may result from the more complex modulation along the ordering vector, which makes it more difficult to order well along this direction.

The half-integer-L (H, K)-maps [Figs. 10(c), (d), (g), (h)] also reproduce the temperature-dependent mSRO around $(\frac{1}{2}, \frac{1}{2})$ positions in Figs. 3 and 4, although the splitting of peaks into pairs at $(\frac{1}{2} \pm \delta, \frac{1}{2} \pm \delta)$ is not observed. The CORELLI data further clearly show that these diffuse scattering are not detectable in higher Brillouin zones, providing strong evidence for their magnetic nature.

Figs. 10(i) and (j) show $(H, -H, L)$-maps for the $x = 0.55$ FCT sample at 7 K and 250 K, respectively. Consistent with observations described so far, the $(\frac{1}{3}, -\frac{1}{3})$ peaks persist at 250 K and are clearly detectable in higher Brillouin zones, whereas the $(\frac{1}{2}, -\frac{1}{2})$ peaks disappear at 250 K and are limited to small momenta. In addition, it can be directly seen that the integer-L $(\frac{1}{3}, -\frac{1}{3})$ peaks occur at slightly smaller momenta compared to the half-integer-L $(\frac{1}{3}, -\frac{1}{3})$ peaks. This is consistent with the HB-1A data in Fig. 6, and is a result of the integer-L peaks being associated with FCT III, which has a slighter larger in-plane d-spacing compared to FCT II [Fig. 9(a)]. These results from the CORELLI data are also confirmed in TOPAZ measurements of a $x = 0.55$ sample at 100 K.

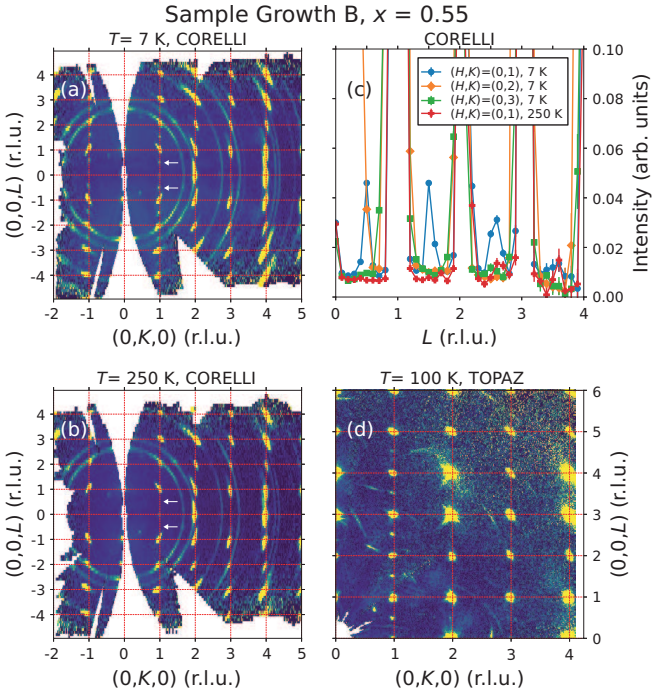

FIG. 11. $(0, K, L)$-maps from the CORELLI data for a $x = 0.55$ FCT sample at (a) 7 K and (b) 250K. The maps are obtained by binning H within ± 0.025. White arrows highlight $(0, 1, \pm\frac{1}{2})$, where sharp magnetic peaks are observed. (c) Comparison of cuts along L obtained from the CORELLI data. The cuts are made by binning H and K within ± 0.025 of the center position. (d) $(0, K, L)$-map of the TOPAZ data for a $x = 0.55$ FCT sample at 100 K. The TOPAZ data has been symmetrized by applying the $H0L$, $HK0$, and $0KL$ mirror planes, and the map is obtained by binning H within ± 0.005.

E. Magnetic order associated with FCT III

The half-integer-L (H, K)-maps of the $x = 0.55$ sample also reveal $(1, 0)/(0, 1)$ peaks that are present at 7 K but not at 250 K [Figs. 10(c), (d), (g), (h)]. The $(0, 1)$ peaks are further confirmed in $(0, K, L)$-maps at 7 K and 250 K [Figs. 11(a) and (b)]. These data show that (i) the $(0, 1)$ peaks appear systematically at half-integer-L positions, (ii) mostly disappear at 250 K, and (iii) equivalent peaks are not detected at $(0, 2)$, $(0, 3)$, or $(0, 4)$. Observations (ii) and (iii) can also be seen in L-cuts of the CORELLI data, shown in Fig. 11(c). These behaviors suggest the half-integer-L $(1, 0)/(0, 1)$ peaks are magnetic. Similar behaviors are also seen in measurements using TOPAZ at 100 K [Fig. 11(d)], further indicating that while these peaks mostly disappear at 250 K, they persist up to at least 100 K.

In addition to the half-integer-L $(1, 0)/(0, 1)$ peaks, Figs. 10(c), (d), (g), (h) also reveal that the half-integer-L $(\frac{1}{3}, \frac{2}{3})$ and $(\frac{2}{3}, \frac{1}{3})$ peaks vary significantly in intensity between 7 K and 250 K. This points to the presence of magnetic peaks at these positions. Given that the half-integer-L $(1, 0)/(0, 1)$ and $(\frac{2}{3}, \frac{1}{3})$ peaks are sharp in momentum and weaken or disappear upon warming to 250 K, they likely have the same origin.

Considering the mSRO signal at half-integer-L $(\frac{1}{2} \pm \delta, \frac{1}{2} \pm \delta)$ appear in FCT samples with x from 0.42 to 0.61, in all of which the half-integer-L $(\frac{1}{3}, \frac{1}{3})$ peaks due to FCT II are detected, we identify the mSRO with FCT II. This identification is consistent with the absence of both half-integer-L $(\frac{1}{2} \pm \delta, \frac{1}{2} \pm \delta)$ magnetic peaks and half-integer-L $(\frac{1}{3}, \frac{1}{3})$ superstructure peaks in the $x = 0.25$ sample [Table. I]. The sharp half-integer-L $(1, 0)/(0, 1)$, $(\frac{1}{3}, \frac{2}{3})$, and $(\frac{2}{3}, \frac{1}{3})$ magnetic peaks in the $x = 0.55$ sample can then be identified with the inter-grown FCT III phase, and is supported by the relatively simple model described below [Fig. 12(b)], which accounts for both the superstructure and magnetic peaks in FCT III.

In the model shown in Fig. 12(b), atoms on the interstitial site are ignored, and Fe-chains are separated by Cu-ladders, leading to the composition $Fe_{1/3}Cu_{2/3}Te$. Fe-Cu ordering in this structure only expands the unit cell in the ab-plane but not along the c-axis, and accounts for the $(\frac{1}{3}, \frac{1}{3})$ superstructure peaks that appear only at integer-L positions. In the superstructure unit cell, which contains only a single Fe atom, the magnetic moments exhibit AFM alignment along a_s, b_s and c (Neel-type magnetic order), which results in magnetic peaks at $(\frac{1}{2}, \frac{1}{2})_s$ positions in the reciprocal space expanded by a_s^* and b_s^* [Fig. 12(c)]. Converting from the scattering pattern in Fig. 12(c) to the reciprocal space associated with the 2-Fe/Cu unit cell in Fig. 1(a), and by further considering a 90 degrees rotated twin domain, leads to the magnetic scattering pattern shown in Fig. 12(d), with magnetic peaks at $(\frac{1}{3}, \frac{2}{3})$, $(\frac{2}{3}, \frac{1}{3})$ and $(1, 0)$ positions. The magnetic peaks appear at half-integer-L positions, due to an AFM alignment of moments along the c-axis.

The model in Fig. 12(b) predicts that magnetic peaks only appear along lines with odd values of $H \pm K$, with $+$ and $-$ corresponding to two domains rotated by 90 degrees [domains B and A in Fig. 12(d), respectively]. The half-integer-L (H, K)-maps in Figs. 10(c), (d), (g), (h) agree remarkably well with the scattering pattern in Fig. 12(d). In particular, temperature-dependent peaks are seen at $(0, 1)$ and $(1, 2)$, but not at $(0, 2)$ and $(-1, 1)$; the $(-\frac{1}{3}, \frac{2}{3})$ and $(-\frac{2}{3}, \frac{1}{3})$ peaks vary strongly with temperature, but the $(-\frac{1}{3}, \frac{1}{3})$ peak hardly changes in intensity between 7 K and 250 K; peaks on the $H + K = 1$ line [solid gray bands in Figs. 10(c) and (d)] vary significantly with temperature, but peaks on the $H + K = 0$ line [dashed gray bands in Figs. 10(c) and (d)] hardly change in intensity between 7 K and 250 K.

The structural and magnetic model in Fig. 12(b) proposed for $Fe_{1/3}Cu_{2/3}Te$ is remarkably similar to that of $NaFe_{0.5}Cu_{0.5}As$ [Fig. 12(a)] [22], both featuring AFM Fe chains separated by Cu atoms. In the proposed structure of $Fe_{1/3}Cu_{2/3}Te$, the magnetic peaks at $(\frac{1}{3}, \frac{2}{3})$, $(\frac{2}{3}, \frac{1}{3})$ arise from superstructure domains that order at integer-L $(\frac{1}{3}, -\frac{1}{3})$ positions, which have Fe chains along [110]. In

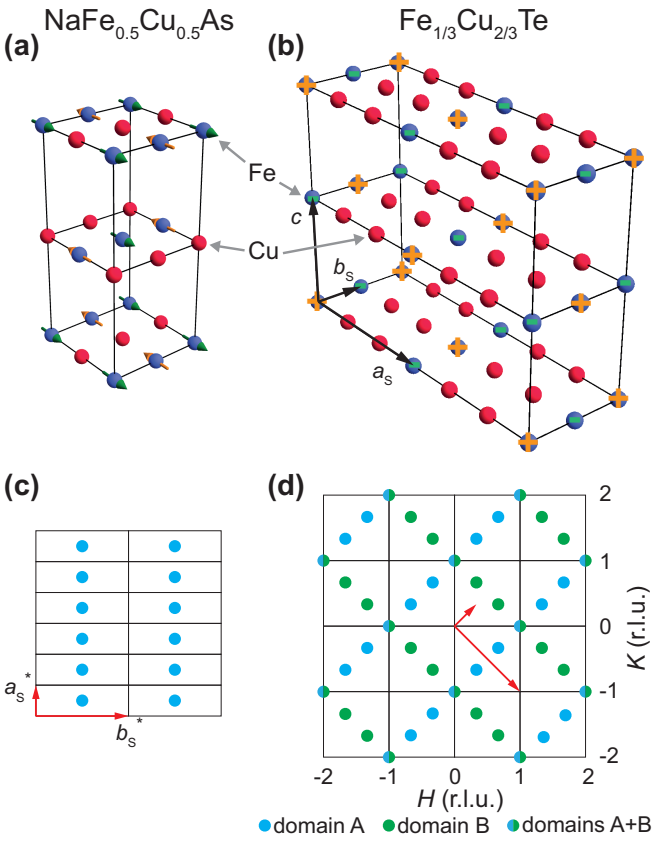

FIG. 12. Schematic crystal and magnetic structures of (a) $NaFe_{0.5}Cu_{0.5}As$ and (b) $Fe_{1/3}Cu_{2/3}Te$, with only Fe and Cu atoms shown. The '+' and '−' symbols represent relative spin orientations of the Fe moments. (c) The expected magnetic peak positions for $Fe_{1/3}Cu_{2/3}Te$, in the reciprocal lattice associated with the superstructure unit cell spanned by a_s and b_s in panel (b). The magnetic peaks appear at $(\frac{1}{2},\frac{1}{2})_s$ and equivalent positions, because the magnetic structure is Neel-type. (d) The magnetic scattering pattern of $Fe_{1/3}Cu_{2/3}Te$, obtained from (c) by translating from the superstructure unit cell spanned by a_s and b_s to the 2-Fe/Cu unit cell in Fig. 1(a), and considering the presence of a domain rotated by 90 degrees.

$NaFe_{0.5}Cu_{0.5}As$, magnetic peaks at $(\frac{1}{2},\frac{1}{2})$ are associated with superstructure domains that order at $(\frac{1}{2},-\frac{1}{2})$, with Fe chains along [110] [22].

F. Exploration of FCT phases via first-principles calculations

To understand the structures of FCT II and FCT III, we studied 5 candidate stoichiometric FCT superstructures via first-principles calculations, without considering occupancy of the interstitial site. These superstructures exhibit $\sqrt{2}\times 3\sqrt{2}$ expansions of the unit cell in the ab-plane relative to $P4/nmm$ FeTe, and include α-$Fe_{2/3}Cu_{1/3}Te$, β-$Fe_{2/3}Cu_{1/3}Te$, $Fe_{1/2}Cu_{1/2}Te$, α-$Fe_{1/3}Cu_{2/3}Te$, and β-$Fe_{1/3}Cu_{2/3}Te$ [Figs. 13(a)-(e), SS1-SS5]. The α phases are AA-stacked with superstructure peaks at integer-L, whereas the β phases are AB-stacked with superstructure peaks at half-integer-L. $Fe_{1/2}Cu_{1/2}Te$ consists of alternating layers with Fe:Cu=1:2 and 2:1, with superstructure peaks at half-integer-L.

We define the formation energies of these compounds as $\Delta E_c(\mathrm{SS}i) = E(\mathrm{SS}i) - ((1-x_i)E_{\mathrm{FeTe}} + x_i E_{\mathrm{CuTe}})$ $(i=1,\cdots,5)$, where x_i is the Cu-content for SSi, $E(\mathrm{SS}i)$ is the energy per formula unit for SSi in DFT calculations, and E_{FeTe} and E_{CuTe} are the energies of $P4/nmm$ FeTe and CuTe. ΔE_c for the 5 superstructures are shown in Fig. 13(f), revealing SS1 and SS5 to be energetically unfavorable. The gray line defines the lowest energy of $Fe_{1-x}Cu_xTe$ compounds for $\frac{1}{3}\le x\le\frac{2}{3}$, when the 5 superstructures in Figs. 13(a)-(e) are considered. As can be seen, SS2 and SS4 fall on the gray line, whereas SS3 has an energy slightly above the gray line.

These first-principles results are consistent with our experimental observation of two inter-grown phases in the FCT phase diagram. Particularly, SS4 is identical to the structure for FCT III inferred from experimental data [Fig. 12(b)], which accounts for both the integer-L superstructure peaks and the sharp half-integer-L magnetic peaks in the $x=0.55$ FCT sample [Figs. 10 and 11]. On the other hand, either SS2 [AB-stacked Fe-ladders separated by Cu-chains] or SS3 [alternating Fe-chains and -ladders separated by Cu-ladders and -chains] may correspond to the FCT II phase with half-integer-L $(\frac{1}{3},\frac{1}{3})$ superstructure peaks and the half-integer-L $(\frac{1}{2}\pm\delta,\frac{1}{2}\pm\delta)$ mSRO peaks. This is because although the energy of SS3 is slightly above the SS2 and SS4 mixture [gray line in Fig. 13(f)], this energy ($\sim$ 1.5 meV) is too small to rule it out in the FCT phase diagram. Although our DFT calculations do not uniquely identify a superstructure for the FCT II phase, the two candidates structures both contain Fe-ladders, making FCT II interesting for the investigation of quantum magnetism and correlated electrons in low dimensions.

IV. DISCUSSION

The $x=0.25$, 0.42, 0.48, 0.58, and 0.61 samples (Growth A) were measured on HB-1A using identical setups, the corresponding data in Figs. 3, 6, 7 are normalized by sample mass, and can be quantitatively compared. The integrated intensities for the $L=0$ and $L=\frac{1}{2}$ superstructure peaks obtained from scans along [110] are shown in Fig. 14(a). The $L=\frac{1}{2}$ peaks are absent in the $x=0.25$ sample, become maximized in the $x=0.42$ and 0.48 samples, and weaken in the $x=0.58$ and 0.61 samples. On the other hand, the $L=0$ peaks are absent in the $x=0.25$, 0.42, and 0.48 samples, first appears in the $x=0.58$ sample, and becomes more intense in the $x=0.61$ sample. Such an evolution suggests a volume-wise competition between FCT II modulated by half-integer-L superstructure peaks, and FCT III modu-

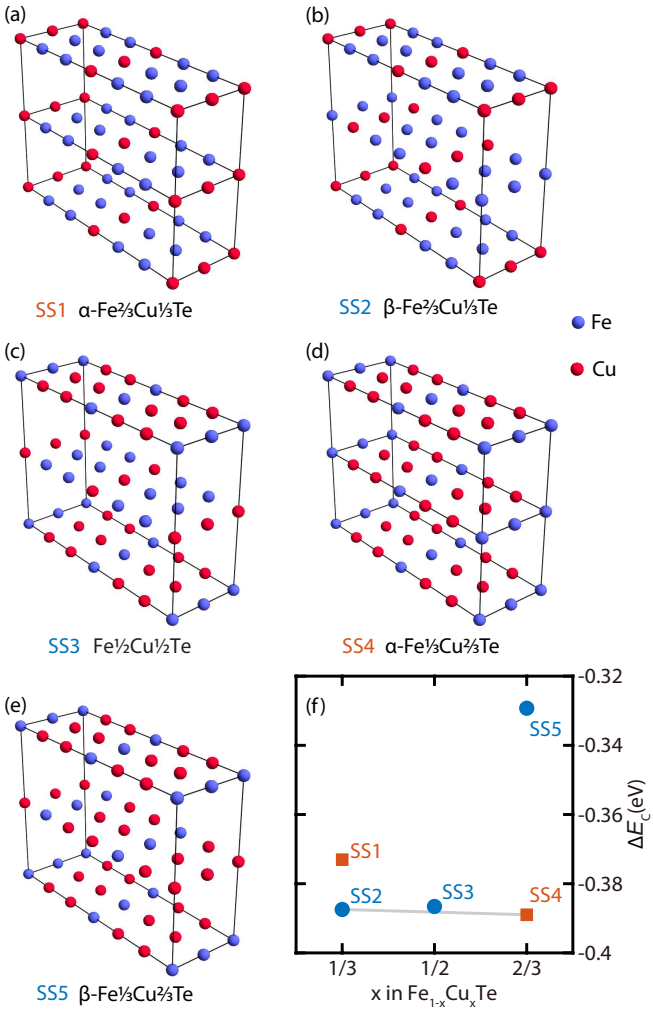

FIG. 13. (a)-(e) The 5 candidate FCT structures considered in DFT calculations, with the interstitial site ignored. Only Fe and Cu atoms shown. (f) The formation energy ΔE_c for the 5 candidate FCT structures, as a function of the Cu-content x. The circle and square symbols represent superstructures that do and do not double the unit cell along the c-axis. The solid gray line represents ΔE_c of the SS2/SS4 mixture, which is slightly below ΔE_c of SS3.

lated by integer-L superstructure peaks.

Fig. 14(b) shows the mSRO intensities as a function of x, obtained by integrating the scans in Fig. 3(c). The magnetic signal first appears in the $x = 0.42$ sample, becomes more intense in the 0.48 sample, and then decreases with further increase of x. Such an evolution with x is similar to the half-integer-L $(\frac{1}{3}, \frac{1}{3})$ superstructure peak, and provides evidence that the mSRO around the stripe-type vector is associated with FCT II.

The superstructure scans at $(\frac{1}{3}, \frac{1}{3}, 0)$ and $(\frac{1}{3}, \frac{1}{3}, \frac{1}{2})$ are fit to Lorentzian peaks [Fig. 8], with the extracted correlation lengths shown in Fig. 14(c). For the half-integer-L $(\frac{1}{3}, \frac{1}{3})$ peak, the in-plane and out-of-plane correlation lengths are highly anisotropic in the $x = 0.42$ and 0.48 samples, with $\xi_{110} \approx 80$ Å and $\xi_c \approx 20$ Å. Increasing x towards 0.58 and 0.62 leads to a reduction in ξ_{110} and an enhancement in ξ_c, so that both are around 40 Å. For the integer-L superstructure peak, both ξ_{110} and ξ_c are enhanced when x is increased from 0.58 to 0.61. In particular, ξ_c for the integer-L superstructure peak in the $x = 0.61$ sample reaches $\sim$ 100 Å, and is (or close to) resolution-limited, with a similar width as a main Bragg peak [Fig. 9(b)].

The in-plane magnetic correlation lengths are obtained by fitting the data in Fig. 3(c) to Eq. 1, and the out-of-plane magnetic correlation lengths are obtained by fitting the data in Fig. 3(d) to a single Lorentzian peak. The extracted magnetic correlation lengths ξ_{110} are roughly in the range $12-18$ Å, and ξ_c roughly in the range $4-9$ Å [Fig. 14(d)], neither changing significantly with x, consistent with the almost overlapping scaled temperature dependence in Fig. 3(f). The x-dependence of the magnetic correlation length contrasts with behaviors of the superstructure correlations lengths, and may result from the former being much shorter, such that it is insensitive to changes in the latter.

The presence of inter-grown phases and significant occupation of the interstitial Fe/Cu site [Table I] in FCT are likely important in accounting for the highly varied sample properties reported in the literature [37–46]. To make further progress in understanding the FCT phase diagram, it is important to synthesize pure phases of the FCT II and FCT III with minimal interstitial Fe/Cu atoms.

The possibility of FCT II realizing Fe-ladders is interesting, given that superconductivity has been found in pressurized Fe-ladder compounds $BaFe_2S_3$ and $BaFe_2Se_3$ [47–49]. Such low-dimensional systems also offer an ideal ground for studying the physics of strongly correlated electrons, since experimental comparisons with realistic models are possible [50–53]. In addition, as single crystals of FCT can be readily made, it offers a potential route towards probing the spin dynamics in multi-orbital chain or ladder systems, whereas the spin dynamics of 123 Fe-ladder systems were mostly carried out on powder samples [54–56]. In the 123 Fe-ladder systems, Fe stoichiometry and sample quality is found to be important for a pressure-induced superconducting state [57]. In this regard, the short-range nature of superstructure and magnetic peaks, the presence of a substantial amount interstitial Fe/Cu atoms, and the presence of the FCT III phase, may be detrimental for achieving a superconducting state. A study of FCT with $x = 0.5$ under pressures up to 34 GPa did not find superconductivity [45].

Our discovery of superstructures in FCT underscore the potential of magnetically diluted iron pnictides and chalcogenides as platforms for realizing low-dimensional correlated electrons and quantum magnetism. Akin to Fe-Cu ordering in $NaFe_{0.5}Cu_{0.5}As$ which leads to Fe chains [22], and Fe-Ag ordering in $KFe_{0.8}Ag_{1.2}Te_2$ that leads to 2×2 Fe blocks exhibiting nematicity [58, 59], this work shows that Fe-Cu ordering in FCT may lead to Fe chains or ladders, although it might be an experimental

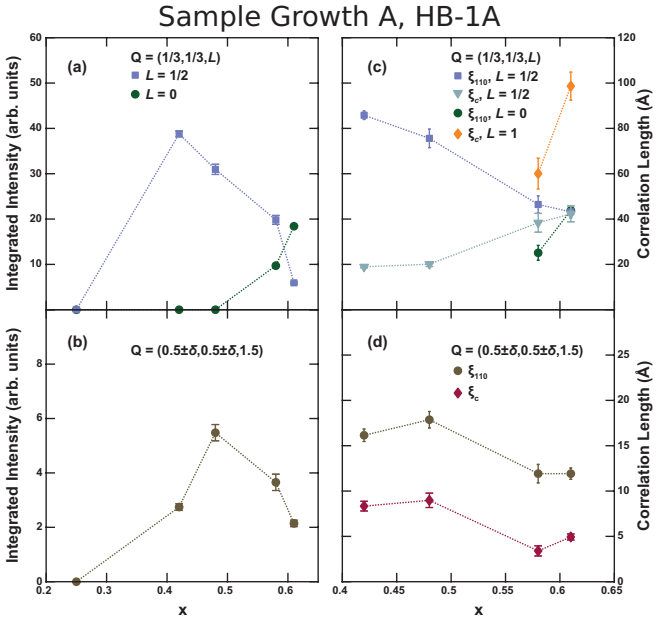

FIG. 14. Doping dependence of (a) $(\frac{1}{3},\frac{1}{3},L)$ superstructure integrated intensities, (b) $(\frac{1}{2}\pm\delta,\frac{1}{2}\pm\delta,\frac{3}{2})$ magnetic peak integrated intensities, (c) $(\frac{1}{3},\frac{1}{3},L)$ superstructure correlation lengths, and (d) $(\frac{1}{2}\pm\delta,\frac{1}{2}\pm\delta,\frac{3}{2})$ magnetic peak correlation lengths. The superstructure correlation lengths are obtained from fits in Fig. 8, and the magnetic correlation lengths are obtained from fits in Figs. 3(c) and (d). Resolution effects have not been considered, and the correlation lengths should be regarded as lower limits.

challenge to achieve perfect ordering between Fe and Cu.

The observation of stripe-type magnetism in FCT II is unexpected, as $Fe_{1+y}Te$ exhibits double-stripe magnetic order with the ordering vector $(\frac{1}{2},0)$ [6, 7]. In combination with previous studies, our results show that while the atomic orderings between Fe atoms and the nonmagnetic ions in $NaFe_{0.5}Cu_{0.5}As$, $KFe_{0.8}Ag_{1.2}Te_2$, $Ba(Fe_{1-x}Cu_x)_2As_2$ and FCT vary, magnetic ordering at or around the stripe-type vector appears common in many of these systems. Given these materials are semiconducting or semiconducting-like, the common magnetism should arise from local moments, therefore localized electronic degrees of freedom may be important for understanding stripe-type magnetism in the FeSCs.

In summary, by carrying out a systematic study of the $(Fe_{1-x}Cu_x)_{1+y}Te$ series using neutron scattering, we discover integer-L and half-integer-L $(\frac{1}{3},\frac{1}{3},0)$ superstructures, associated with two distinct phases (FCT II and III respectively). Diffuse half-integer-L $(\frac{1}{2}\pm\delta,\frac{1}{2}\pm\delta)$ $(\delta\approx0.05)$ magnetic peaks are detected around the stripe-type ordering vector, identified with the FCT II phase. Sharp half-integer-L $(\frac{1}{3},\frac{2}{3})$, $(\frac{2}{3},\frac{1}{3})$ and $(1,0)$ magnetic peaks are observed in a $x=0.55$ sample, resulting from the FCT III phase inter-grown with FCT II. We explore possible structures of FCT II and FCT III via first-principles calculations, finding that FCT III consists of Fe-chains and FCT II contains Fe-ladders. The commonality of stripe-type magnetism in several magnetically diluted Fe pnictide and chalcogenide compounds indicate such magnetism could arise from localized electronic degrees of freedom. Furthermore, our findings highlight magnetically diluted Fe pnictides and chalcogenides as promising platforms for studying low-dimensional correlated electrons and quantum magnetism.

The work at Zhejiang University was supported by the Pioneer and Leading Goose R&D Program of Zhejiang (2022SDXHDX0005), the National Key R&D Program of China (No. 2022YFA1402200), the Key R&D Program of Zhejiang Province, China (2021C01002), and the National Science Foundation of China (No. 12274363 and No. 12274364). The work at University of California, Berkeley and Lawrence Berkeley National Laboratory was supported by the Office of Science, Office of BES, Materials Sciences and Engineering Division, of the U.S. DOE under Contract No. DE-AC02-05-CH11231 within the Quantum Materials Program (KC2202). A portion of this research used resources at the High Flux Isotope Reactor (HFIR) and Spallation Neutron Source (SNS), which are DOE Office of Science User Facilities operated by the Oak Ridge National Laboratory (ORNL).

* yusong_phys@zju.edu.cn

[1] D. J. Scalapino, Rev. Mod. Phys. **84**, 1383 (2012).
[2] P. Dai, Rev. Mod. Phys. **87**, 855 (2015).
[3] G. R. Stewart, Rev. Mod. Phys. **83**, 1589 (2011).
[4] J. Wen, Annals of Physics **358**, 92 (2015).
[5] J. M. Tranquada, G. Xu, and I. A. Zaliznyak, Journal of Physics: Condensed Matter **32**, 374003 (2020).
[6] W. Bao, Y. Qiu, Q. Huang, M. A. Green, P. Zajdel, M. R. Fitzsimmons, M. Zhernenkov, S. Chang, M. Fang, B. Qian, E. K. Vehstedt, J. Yang, H. M. Pham, L. Spinu, and Z. Q. Mao, Phys. Rev. Lett. **102**, 247001 (2009).
[7] S. Li, C. de la Cruz, Q. Huang, Y. Chen, J. W. Lynn, J. Hu, Y.-L. Huang, F.-C. Hsu, K.-W. Yeh, M.-K. Wu, and P. Dai, Phys. Rev. B **79**, 054503 (2009).
[8] D. J. Singh and M.-H. Du, Phys. Rev. Lett. **100**, 237003 (2008).
[9] I. I. Mazin, Nature **464**, 183 (2010).
[10] Q. Si and E. Abrahams, Phys. Rev. Lett. **101**, 076401 (2008).
[11] W.-G. Yin, C.-C. Lee, and W. Ku, Phys. Rev. Lett. **105**, 107004 (2010).
[12] P. C. Canfield and S. L. Bud'ko, Annual Review of Condensed Matter Physics **1**, 27 (2010).
[13] H.-H. Wen and S. Li, Annual Review of Condensed Matter Physics **2**, 121 (2011).
[14] M. G. Kim, J. Lamsal, T. W. Heitmann, G. S. Tucker, D. K. Pratt, S. N. Khan, Y. B. Lee, A. Alam, A. Thaler, N. Ni, S. Ran, S. L. Bud'ko, K. J. Marty, M. D. Lumsden, P. C. Canfield, B. N. Harmon, D. D. Johnson, A. Kreyssig, R. J. McQueeney, and A. I. Goldman, Phys.

Rev. Lett. **109**, 167003 (2012).
[15] S. Ideta, T. Yoshida, I. Nishi, A. Fujimori, Y. Kotani, K. Ono, Y. Nakashima, S. Yamaichi, T. Sasagawa, M. Nakajima, K. Kihou, Y. Tomioka, C. H. Lee, A. Iyo, H. Eisaki, T. Ito, S. Uchida, and R. Arita, Phys. Rev. Lett. **110**, 107007 (2013).
[16] N. Ni, A. Thaler, J. Q. Yan, A. Kracher, E. Colombier, S. L. Bud'ko, P. C. Canfield, and S. T. Hannahs, Phys. Rev. B **82**, 024519 (2010).
[17] A. F. Wang, J. J. Lin, P. Cheng, G. J. Ye, F. Chen, J. Q. Ma, X. F. Lu, B. Lei, X. G. Luo, and X. H. Chen, Phys. Rev. B **88**, 094516 (2013).
[18] S. T. Cui, S. Kong, S. L. Ju, P. Wu, A. F. Wang, X. G. Luo, X. H. Chen, G. B. Zhang, and Z. Sun, Phys. Rev. B **88**, 245112 (2013).
[19] Y. J. Yan, P. Cheng, J. J. Ying, X. G. Luo, F. Chen, H. Y. Zou, A. F. Wang, G. J. Ye, Z. J. Xiang, J. Q. Ma, and X. H. Chen, Phys. Rev. B **87**, 075105 (2013).
[20] C. Ye, W. Ruan, P. Cai, X. Li, A. Wang, X. Chen, and Y. Wang, Phys. Rev. X **5**, 021013 (2015).
[21] C. E. Matt, N. Xu, B. Lv, J. Ma, F. Bisti, J. Park, T. Shang, C. Cao, Y. Song, A. H. Nevidomskyy, P. Dai, L. Patthey, N. C. Plumb, M. Radovic, J. Mesot, and M. Shi, Phys. Rev. Lett. **117**, 097001 (2016).
[22] Y. Song, Z. Yamani, C. Cao, Y. Li, C. Zhang, J. S. Chen, Q. Huang, H. Wu, J. Tao, Y. Zhu, W. Tian, S. Chi, H. Cao, Y.-B. Huang, M. Dantz, T. Schmitt, R. Yu, A. H. Nevidomskyy, E. Morosan, Q. Si, and P. Dai, Nature Communications **7**, 10.1038/ncomms13879 (2016).
[23] A. Charnukha, Z. P. Yin, Y. Song, C. D. Cao, P. Dai, K. Haule, G. Kotliar, and D. N. Basov, Phys. Rev. B **96**, 195121 (2017).
[24] Y. Xin, I. Stolt, Y. Song, P. Dai, and W. P. Halperin, Phys. Rev. B **101**, 064410 (2020).
[25] M. G. Kim, M. Wang, G. S. Tucker, P. N. Valdivia, D. L. Abernathy, S. Chi, A. D. Christianson, A. A. Aczel, T. Hong, T. W. Heitmann, S. Ran, P. C. Canfield, E. D. Bourret-Courchesne, A. Kreyssig, D. H. Lee, A. I. Goldman, R. J. McQueeney, and R. J. Birgeneau, Phys. Rev. B **92**, 214404 (2015).
[26] W. Wang, Y. Song, D. Hu, Y. Li, R. Zhang, L. W. Harriger, W. Tian, H. Cao, and P. Dai, Phys. Rev. B **96**, 161106 (2017).
[27] J. Wen, Z. Xu, G. Xu, M. D. Lumsden, P. N. Valdivia, E. Bourret-Courchesne, G. Gu, D.-H. Lee, J. M. Tranquada, and R. J. Birgeneau, Phys. Rev. B **86**, 024401 (2012).
[28] H. Wang, C. Dong, Z. Li, J. Yang, Q. Mao, and M. Fang, Physics Letters A **376**, 3645 (2012).
[29] P. N. Valdivia, M. G. Kim, T. R. Forrest, Z. Xu, M. Wang, H. Wu, L. W. Harringer, E. D. Bourret-Courchesne, and R. J. Birgeneau, Phys. Rev. B **91**, 224424 (2015).
[30] T. Helm, P. N. Valdivia, E. Bourret-Courchesne, J. G. Analytis, and R. J. Birgeneau, Journal of Physics: Condensed Matter **29**, 285801 (2017).
[31] G. Kresse and J. Hafner, Phys. Rev. B **47**, 558 (1993).
[32] G. Kresse and D. Joubert, Phys. Rev. B **59**, 1758 (1999).
[33] P. E. Blöchl, Phys. Rev. B **50**, 17953 (1994).
[34] J. P. Perdew, K. Burke, and M. Ernzerhof, Phys. Rev. Lett. **77**, 3865 (1996).
[35] D. K. Pratt, M. G. Kim, A. Kreyssig, Y. B. Lee, G. S. Tucker, A. Thaler, W. Tian, J. L. Zarestky, S. L. Bud'ko, P. C. Canfield, B. N. Harmon, A. I. Goldman, and R. J. McQueeney, Phys. Rev. Lett. **106**, 257001 (2011).
[36] H. Luo, R. Zhang, M. Laver, Z. Yamani, M. Wang, X. Lu, M. Wang, Y. Chen, S. Li, S. Chang, J. W. Lynn, and P. Dai, Phys. Rev. Lett. **108**, 247002 (2012).
[37] A. A. Vaipolin, S. A. Kijaev, L. V. Kradinova, A. M. Polubotko, V. V. Popov, V. D. Prochukhan, Y. V. Rud, and V. E. Skoriukin, Journal of Physics: Condensed Matter **4**, 8035 (1992).
[38] J. Llanos and C. Mujica, Journal of Alloys and Compounds **217**, 250 (1995).
[39] A. Rivas, F. Gonzalez-Jimenez, L. D'Onofrio, E. Jaimes, M. Quintero, and J. Gonzalez, Hyperfine Interactions **113**, 493 (1998).
[40] A.-M. Lamarche, J. Woolley, G. Lamarche, I. Swainson, and T. Holden, Journal of Magnetism and Magnetic Materials **186**, 121 (1998).
[41] F. Gonzalez-Jimenez, E. Jaimes, A. Rivas, L. D'Onofrio, J. Gonzalez, and M. Quintero, Physica B: Condensed Matter **259-261**, 987 (1999).
[42] A. Rivas, F. Gonzalez-Jimenez, L. D'Onofrio, E. Jaimes, M. Quintero, and J. Gonzalez, Hyperfine Interactions **134**, 115 (2001).
[43] A. I. Dzhabbarov, S. K. Orudzhev, G. G. Guseinov, and N. F. Gakhramanov, Crystallography Reports **49**, 1038 (2004).
[44] F. N. Abdullaev, T. G. Kerimova, G. D. Sultanov, and N. A. Abdullaev, Physics of the Solid State **48**, 1848 (2006).
[45] D. A. Zocco, D. Y. Tütün, J. J. Hamlin, J. R. Jeffries, S. T. Weir, Y. K. Vohra, and M. B. Maple, Superconductor Science and Technology **25**, 084018 (2012).
[46] V. V. Popov, P. P. Konstantinov, and Y. V. Rud', Journal of Experimental and Theoretical Physics **113**, 683 (2011).
[47] H. Takahashi, A. Sugimoto, Y. Nambu, T. Yamauchi, Y. Hirata, T. Kawakami, M. Avdeev, K. Matsubayashi, F. Du, C. Kawashima, H. Soeda, S. Nakano, Y. Uwatoko, Y. Ueda, T. J. Sato, and K. Ohgushi, Nature Materials **14**, 1008 (2015).
[48] T. Yamauchi, Y. Hirata, Y. Ueda, and K. Ohgushi, Phys. Rev. Lett. **115**, 246402 (2015).
[49] J. Ying, H. Lei, C. Petrovic, Y. Xiao, and V. V. Struzhkin, Phys. Rev. B **95**, 241109 (2017).
[50] E. Dagotto and T. M. Rice, Science **271**, 618 (1996).
[51] J. Herbrych, N. Kaushal, A. Nocera, G. Alvarez, A. Moreo, and E. Dagotto, Nature Communications **9**, 10.1038/s41467-018-06181-6 (2018).
[52] S. Wu, B. A. Frandsen, M. Wang, M. Yi, and R. Birgeneau, Journal of Superconductivity and Novel Magnetism **33**, 143 (2019).
[53] Z. Chen, Y. Wang, S. N. Rebec, T. Jia, M. Hashimoto, D. Lu, B. Moritz, R. G. Moore, T. P. Devereaux, and Z.-X. Shen, Science **373**, 1235 (2021).
[54] M. Mourigal, S. Wu, M. B. Stone, J. R. Neilson, J. M. Caron, T. M. McQueen, and C. L. Broholm, Phys. Rev. Lett. **115**, 047401 (2015).
[55] M. Wang, M. Yi, S. Jin, H. Jiang, Y. Song, H. Luo, A. D. Christianson, C. de la Cruz, E. Bourret-Courchesne, D.-X. Yao, D. H. Lee, and R. J. Birgeneau, Phys. Rev. B **94**, 041111 (2016).
[56] M. Wang, S. J. Jin, M. Yi, Y. Song, H. C. Jiang, W. L. Zhang, H. L. Sun, H. Q. Luo, A. D. Christianson, E. Bourret-Courchesne, D. H. Lee, D.-X. Yao, and R. J. Birgeneau, Phys. Rev. B **95**, 060502 (2017).
[57] H. Sun, X. Li, Y. Zhou, J. Yu, B. A. Frandsen, S. Wu,

Z. Xu, S. Jiang, Q. Huang, E. Bourret-Courchesne, L. Sun, J. W. Lynn, R. J. Birgeneau, and M. Wang, Phys. Rev. B **101**, 205129 (2020).
[58] Y. Song, H. Cao, B. C. Chakoumakos, Y. Zhao, A. Wang, H. Lei, C. Petrovic, and R. J. Birgeneau, Phys. Rev. Lett. **122**, 087201 (2019).
[59] Y. Song, D. Yuan, X. Lu, Z. Xu, E. Bourret-Courchesne, and R. J. Birgeneau, Phys. Rev. Lett. **123**, 247205 (2019).